Enhanced spin-flip scattering by surface roughness in WS$_2$ and MoS$_2$ armchair nanoribbons

Shoeib Babaee Touski,[1,2] Rafael Roldán,[3,*] Mahdi Pourfath,[1,4,†] and M. Pilar López-Sancho[3]

[1]*School of Electrical and Computer Engineering, University of Tehran, Tehran 14395-515, Iran*
[2]*Department of Electrical Engineering, Hamedan University of Technology, Hamedan 65155, Iran*
[3]*Instituto de Ciencia de Materiales de Madrid, CSIC, E-28049 Cantoblanco, Madrid, Spain*
[4]*School of Nano Science, Institute for Research in Fundamental Sciences (IPM), Tehran 19395-5531, Iran*

The band structures of single-layer MoS$_2$ and WS$_2$ present a coupling between spin and valley degrees of freedom that suppresses spin-flip scattering and spin dephasing. Here we show that out-of-plane deformations, such as corrugations or ripples, enhance spin-flip scattering in armchair MoS$_2$ and WS$_2$ nanoribbons. Spin transport in the presence of surface roughness is systematically investigated, employing the nonequilibrium Green's function method along with the tight-binding approximation. Both transmission and conductance have been calculated as a function of surface roughness. Our results indicate that the spin-flip rate, usually neglected in flat pristine samples, increases significantly with the surface roughness amplitude. These results are important for the design and fabrication of transition metal dichalcogenides based spintronic devices.

I. INTRODUCTION

A long spin relaxation length, i.e., the possibility for spin-polarized electrons to travel larger distances without losing encoded information, is a basic requirement for spintronic applications. Graphene was envisioned early on as a promising material for spintronics, owing to the combination of the unique electronic band structure of so-called massless Dirac fermions, weakly sensitive to backscattering and traveling at very high speed over very large distances, even at room temperature [1,2]. However the weak spin-orbit coupling (SOC) in graphene makes spin effects very small. The discovery of graphene paved the way for investigating other two-dimensional (2D) materials with properties complementary to those of graphene [3]. Stacking of different families of 2D materials in a controlled fashion can create heterostructures with tailored properties that offer promising avenues to design and fabricate novel devices [4].

Single layers of transition-metal dichalcogenides (TMDCs) such as MoS$_2$ and WS$_2$ are direct band gap semiconductors with strong spin-orbit coupling, which originates from *d* orbitals of the heavy transition-metal atoms. This allows for the control of spin with electric field [5–10]. The band structure of TMDC consists of two inequivalent valleys (K and K′) located at the corners of the hexagonal Brillouin zone [11]. The lack of inversion symmetry alongside the large SOC strength lead to the coupling of spin and valley degrees of freedom [12], allowing for spin and valley control with the potential use of TMDCs in valleytronics and spintronics [13–16]. Magnetotransport experiments have estimated an upper limit for the spin-orbit scattering length for *n*-type MoS$_2$ as high as 430 nm [17]. However, mirror symmetry along the *z* direction is usually broken due to surface ripples, thermal out-of-plane fluctuations, sulfur vacancies, etc., which leads to a Rashba-like spin-orbit contribution, which can limit the spin lifetime [18]. In particular, static wrinkles have been shown to affect more the spin coherence as compared to out-of-plane phonons [19].

Nanoribbons of TMDCs can be obtained by tailoring a ribbon from an infinitely extended monolayer [20], and can be synthesized by using electrochemical methods [21], or by unzipping nanotubes [22–24]. First-principles calculations indicate that armchair MoS$_2$ and WS$_2$ nanoribbons show semiconducting behavior, while zigzag nanoribbons are metallic [25,26]. In this work we study the effect of surface corrugation on spin transport in armchair nanoribbons of MoS$_2$ and WS$_2$ (Fig. 1). For this we use nonequilibrium Green's function formalism along with a tight-binding model applied to nanoribbons of TMDCs in the presence of surface roughness. We find a significant increase of spin-flip rate due to static corrugations of the sample. The effects are more important in WS$_2$ than in MoS$_2$, due to the stronger atomic SOC of W atoms. Our results suggest that the use of flat substrates can considerably increase the efficiency of TMDCs for spintronics applications.

The paper is organized as follows. In Sec. II we describe the model and the calculation method, taking into account surface roughness effects. In Sec. III the results are presented and discussed. Finally, in Sec. IV the main conclusions are summarized. In Appendix we present results obtained considering periodic boundary conditions.

II. MODEL AND METHOD

A. Tight-binding Hamiltonian

The crystal structure of TMDCs consist of one triangular lattice of metal atoms (Mo or W in the present case), which is sandwiched between two triangular lattices of chalcogen (S) atoms. Thus, the unit cell contains one transition-metal atom plus two chalcogen atoms. Our calculations will be performed by using a tight-binding model that contains five *d* orbitals of the metal (Mo/W) atoms and three *p* orbitals for each of the two chalcogen S atoms in the unit cell [27]. Therefore, the dimension of the Hamiltonian of a single layer (before including spin degrees of freedom) will be 11×11, and can

---
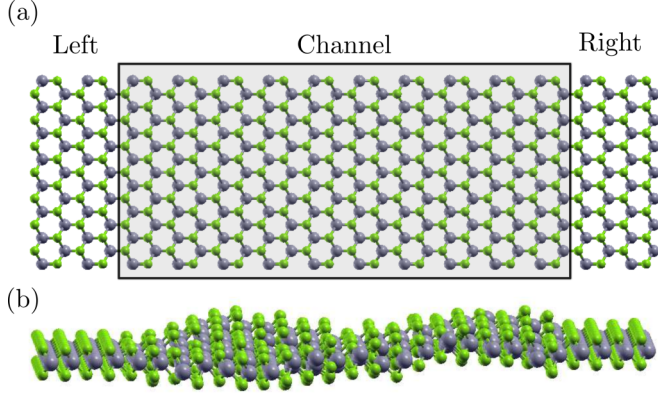*rroldan@icmm.csic.es
†pourfath@ut.ac.ir

(a)

(b)

FIG. 1. Sketch of the system considered in our calculations. (a) Channel and leads are made of the same family of TMDC, MoS_2 or WS_2. (b) Surface roughness is considered for the channel sector, but not for the leads.

be written as:

$$\hat{H}_0 = \sum_{i;l} \epsilon_{i;l} \hat{c}_{i;l}^\dagger \hat{c}_{i;l} + \sum_{\langle i,j \rangle;l,m} V_{i,j;l,m} \hat{c}_{i;l}^\dagger \hat{c}_{j;m}, \qquad (1)$$

where i,j are the atomic position indices, l and m label the atomic orbitals, $\hat{c}_{i;l}^\dagger(\hat{c}_{i;l})$ creates (annihilates) an electron at orbital l of site i, $\epsilon_{i;l}$ refers to on-site crystal fields of orbital l and $V_{i,j;l,m}$ are hopping parameters, where $\langle ij \rangle$ runs over first-nearest-neighbor sites. The Slater-Koster parameters for MoS_2 and WS_2 obtained from fits to density functional theory (DFT) calculations are reported in Table I [28]. The ratio of the metal d and chalcogen p orbital contributions to the valence and conduction bands in our tight-binding model is ∼70/30 respectively, in good agreement with DFT calculations [27]. By performing a unitary transformation that accounts for the symmetric and antisymmetric combinations of S-p orbitals of the top and bottom chalcogen atoms, it is possible to simplify the model into two decoupled blocks of dimensions 6×6 and 5×5, being the 6×6 block the relevant

TABLE I. Spin-orbit coupling λ_α and tight-binding parameters for single-layer MS_2, where the metal M is Mo or W. All the Slater-Koster parameters are in units of eV.

		MoS$_2$	WS$_2$
SOC	λ_M	0.075	0.215
	λ_S	0.052	0.057
Crystal fields	$\epsilon_{d_{3z^2-r^2}}$	−1.094	−0.872
	$\epsilon_{d_{xz}}, \epsilon_{d_{yz}}$	0.670	0.670
	$\epsilon_{d_{xy}}, \epsilon_{d_{x^2-y^2}}$	−1.511	−1.511
	$\epsilon_{p_x}, \epsilon_{p_y}$	−3.559	−3.468
	ϵ_{p_z}	−6.886	−3.913
M-S	$V_{pd\sigma}$	3.689	3.603
	$V_{pd\pi}$	−1.241	−0.942
M-M	$V_{dd\sigma}$	−0.895	−1.216
	$V_{dd\pi}$	0.252	0.177
	$V_{dd\delta}$	0.228	0.243
S-S	$V_{pp\sigma}$	1.225	0.749
	$V_{pp\pi}$	−0.467	0.236

subspace for low-energy calculations since it contains the valence and conduction band states. The bases of these blocks are $(d_{xy}, d_{x^2-y^2}, d_{3z^2-r^2}, p_x^S, p_y^S, p_z^A)$ and $(d_{xz}, d_{yz}, p_x^A, p_y^A, p_z^S)$, respectively [27], where A and S stand for the symmetric and antisymmetric combinations of the top t and bottom b chalcogen p orbitals, $p_i^{S(A)} = 1/\sqrt{2}(p_i^t \pm p_i^b)$, where $i = x, y, z$.

Spin-orbit coupling, however, mixed these blocks through processes that flip the electron spin [29]. The SOC contribution is included in our theory trough the term

$$\hat{H}_{SO} = \sum_{i;l,m} \frac{\lambda_{i;l,m}}{\hbar} \hat{L}_{i;l} \cdot \hat{S}_{i;m}, \qquad (2)$$

where λ is the intra-atomic SOC constant, $\hat{L}$ is the angular momentum operator for atomic orbitals, and $\hat{S}$ is the spin operator. It is useful to express $\hat{H}_{SO}$ as:

$$\hat{H}_{SO} = \sum_{i;l,m} \frac{\lambda_{i;l}}{\hbar} \left[\frac{\hat{L}_{i;l}^+ \hat{S}_{i;m}^- + \hat{L}_{i;l}^- \hat{S}_{i;m}^+}{2} + \hat{L}_{i;l}^z \hat{S}_{i;m}^z \right], \qquad (3)$$

where $\hat{O}^\pm = \hat{O}^x \pm i \hat{O}^y$ are the standard ladder operators, with $\hat{O} = \hat{L}, \hat{S}$. We can distinguish two different contributions to the SOC Hamiltonian (3), the first term, which leads to spin-flip processes, and the spin-conserving term $\propto \lambda \hat{L}^z \hat{S}^z$. For flat pristine MoS_2 or WS_2, spin-flip processes are negligible and full spin polarization as well as long spin relaxation lengths can be achieved [30]. In this limit one can safely reduce to the 6×6 block [29]. However, as experimentally observed [31,32] realistic samples do not preserve mirror symmetry along the z direction. This is due to the presence of sulfur vacancies, or to corrugations and ripples in the sample, associated, e.g., to the presence of a substrate or due to thermal out-of-plane phonons. In this situation, the 6×6 and the 5×5 blocks are coupled. As a consequence, the contribution of d_{xz} and d_{yz} orbitals to the density of states (DOS) of the corrugated ribbon is significantly larger than in the flat situation. Importantly, spin-flip processes become relevant, limiting spin lifetime [18]. Therefore, we will use in our calculations the whole Hilbert space of dimension 2×11 (including spin). We notice that, contrary to previous works that consider the effect of flexural phonons, corrugations or topological defects in the transport properties from minimal $\mathbf{k} \cdot \mathbf{p}$ models and group theory methods [16,33], here we use a tight-binding model that accurately accounts for the states of the valence and conduction bands in the whole Brillouin zone, to calculate spin-resolved transmission probabilities through a finite corrugated armchair ribbon of MoS_2 or WS_2.

B. Nonequilibrium Green's function method

The nonequilibrium Green's function (NEGF) formalism [34] is used to study spin transport in armchair MoS_2 and WS_2 nanoribbons. The channel and the two contacts are assumed to be of the same material (see Fig. 1). For the calculation of the contact self-energies, the surface Green's function of the contacts is iteratively solved, employing a highly convergent scheme [35,36]

$$\underline{g}^{L,R} = \left[E\underline{I} - \underline{H}^{L,R} - \underline{h}_c^{L,R} \underline{g}^{L,R} (\underline{\tau}_c^{L,R})^\dagger \right]^{-1}, \qquad (4)$$

where E is the energy, $\underline{I}$ is the identity matrix, $\underline{H}^{L,R}$ is the Hamiltonian of the unit cell of the right or left contact in real-space representation, $\underline{h}_c^{L,R}$ is the coupling between two neighboring unit cells in the considered contacts, and $\underline{\tau}_c^{L,R}$ is the coupling between the channel and the contacts. Underlined quantities stand for matrices that include both spins. A flat interface is assumed in the contacts, and our calculations include SOC in the channel as well as in the leads. The retarded $\underline{G}^r$ and advanced $\underline{G}^a$ Green's functions of the device region are then given by:

$$\underline{G}^r(E) = [(E + i\delta)\underline{I} - \underline{H} - \underline{\Sigma}^L - \underline{\Sigma}^R]^{-1},$$
$$\underline{G}^a(E) = [(E - i\delta)\underline{I} - \underline{H} - \underline{\Sigma}^L - \underline{\Sigma}^R]^{-1}, \quad (5)$$

where δ is a phenomenological broadening (10^{-5}eV), and $\Sigma_\sigma^{L,R}$ is the self-energy of the left and right contacts

$$\Sigma_\sigma^{L,R} = \tau_\sigma^{L,R} g_\sigma^{L,R} (\tau_\sigma^{L,R})^\dagger, \quad (6)$$

where $g_\sigma^{L,R}$ is the surface Green's function of the contacts, given by Eq. (4). The transmission probability is given by

$$T(E) = \text{Tr}[\underline{\Gamma}^L \underline{G}^r \underline{\Gamma}^R \underline{G}^a], \quad (7)$$

where $\underline{\Gamma}^{L,R} = i(\underline{\Sigma}^{L,R} - (\underline{\Sigma}^{L,R})^\dagger)$ describes the broadening of the two semi-infinite leads. The spin-resolved transmission probability can be written as:

$$T_{\sigma\sigma'}(E) = \text{Tr}[\Gamma_\sigma^L G_{\sigma\sigma'}^r \Gamma_{\sigma'}^R G_{\sigma'\sigma}^a], \quad \sigma,\sigma' = \uparrow,\downarrow, \quad (8)$$

where $T_{\uparrow\uparrow}(E)$ and $T_{\downarrow\downarrow}(E)$ represent parallel spin transmission, and $T_{\uparrow\downarrow}(E)$ and $T_{\downarrow\uparrow}(E)$ antiparallel spin-flip transmission.

C. Effect of lattice modulation

Different modulations of the lattice have been studied, as bending, sinusoidal ripples, and Gaussian corrugation. Here we present results for the Gaussian corrugation although some comments to the other type of disorder will be made. The surface roughness of the substrate is modeled by a Gaussian autocorrelation function [37,38]:

$$R(x,y) = \delta h^2 \exp\left(-\frac{x^2}{L_x^2} - \frac{y^2}{L_y^2}\right), \quad (9)$$

where L_x and L_y are the roughness correlation lengths along the x and y directions, respectively, and δh is the root mean square of the variation amplitude. We use in most of our calculations $L_x = L_y = 40$ nm. Typical roughness parameters for several common substrate materials are reported in Table II. As compared to the well-studied case of graphene, we notice that the larger bending rigidity of MoS$_2$ causes smoother surface roughness and longer correlation lengths. Surface roughness modulates atomic positions and orbital directions, thus affecting the hopping parameters.

TABLE II. The root mean square of surface roughness for TMDCs on various substrates [43–48].

SiO$_2$	Mica	h-BN	Al$_2$O$_3$
108–420 pm	77 pm	63 pm	140–390 pm

The effect of lattice deformations due to corrugation are considered within our Slater-Koster tight-binding model. If we neglect the corrections to the on-site potentials due to lattice deformation, the effect of strain is thus considered by varying the interatomic bond lengths as a result of the applied strain. The modified hopping terms in the modulated lattice can be written, at the leading order, as

$$V_{i,j;l,m}(\mathbf{r}_{ij}) = V_{i,j;l,m}(\mathbf{r}_{ij}^0)\left(1 - \beta_{i,j;l,m}\frac{|\mathbf{r}_{ij} - \mathbf{r}_{ij}^0|}{|\mathbf{r}_{ij}^0|}\right), \quad (10)$$

where $|\mathbf{r}_{ij}^0|$ is the distance between two atoms labeled by i and j in the unperturbed lattice, $|\mathbf{r}_{ij}|$ the separation in the presence of corrugation, and $\beta_{i,j;l,m} = -d \ln V_{i,j;l,m}(r)/d \ln(r)|_{r=|\mathbf{r}_{ij}^0|}$ is the dimensionless bond-resolved local electron-phonon coupling, where l and m are the considered orbitals in atoms i and j. The lattice distances are $|\mathbf{r}_{ij}^0| = a$ for the in-plane M-M and X-X bonds, where a is the in-plane interatomic distance, and $|\mathbf{r}_{ij}^0| = \sqrt{7/12}a$ for the M-X bond. In the absence of any theoretical and experimental estimation for the electron-phonon coupling, we adopt the Wills-Harrison argument [39], assuming that $\beta_{i,j;l,m}$ depend solely on the total angular momentum of the l and m orbitals, not on their L^z projections. Namely, $V_{i,j;l,m}(r) \propto |\mathbf{r}|^{-(\ell_l+\ell_m+1)}$, where ℓ_l is the absolute value of the angular momentum of the orbital l, and ℓ_m is the absolute value of the angular momentum of the orbital m. Following this approach we assume that $\beta_{i,j;p-p} = 3$, $\beta_{i,j;p-d} = 4$, and $\beta_{i,j;d-d} = 5$, for the X-X pp, for X-M pd, and for the M-M dd hybridizations, respectively. This approximation has been successfully applied to the study of TMDCs in the presence of nonuniform profiles of strain [28,40]. Importantly, this set of parameters matches the direct-to-indirect band-gap transition in MoS$_2$ under 2–3% of biaxial strain as obtained from *ab initio* calculations [41,42].

As explained in Sec. II A, we consider here an intrinsic SOC term in the whole Brillouin zone, including both metal d and chalcogen p orbitals. This term given by Eq. (3) includes all the spin contributions arising from the crystal potential. The spin-flip terms of the SOC, as discussed before, are negligible in the flat geometries. In the corrugated ribbon, the break of the mirror symmetry produces nonzero matrix elements between the even and odd blocks of the Hamiltonian and therefore spin-flip terms of the $\hat{H}_{SO}$ become significative. In the rest of the paper we present the results for the spin transport properties of corrugated TMDC ribbons obtained by using the above numerical methods.

III. RESULTS AND DISCUSSION

In graphene, it is known that surface roughness mixes π with σ bonds, what enhances spin-orbit interaction [49–51]. In the following we will show which is the effect of sample corrugations on the charge and spin transport properties of TMDCs. The band structure of a MoS$_2$ armchair nanoribbon is shown in Fig. 2(a). In agreement with density functional theory (DFT) calculations [25,26], our tight-binding model for the ribbon with this termination shows a semiconducting behavior, with the appearance of edge states inside the gap, that would be absent if periodic boundary conditions are considered. These edge-state sub-bands are marked in Fig. 2(a). It is important
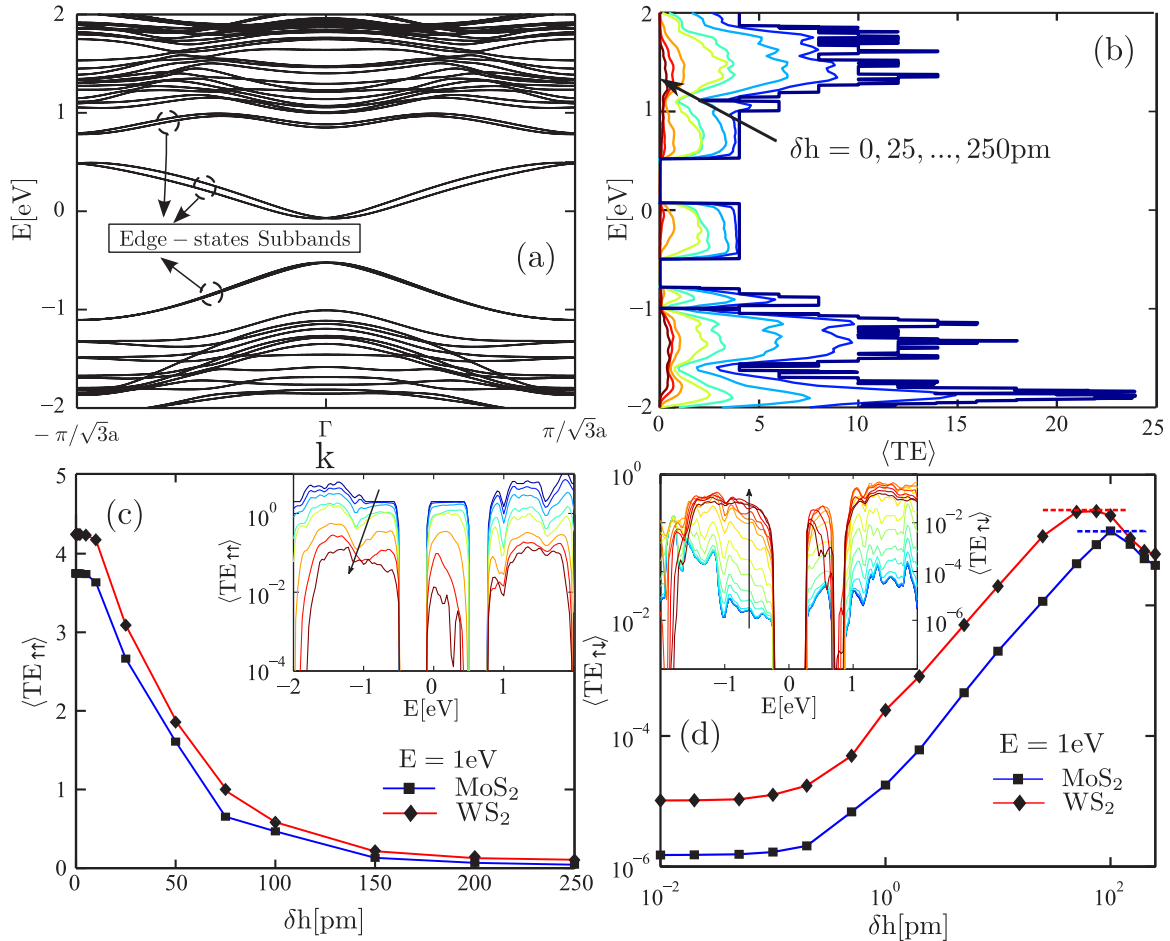
FIG. 2. (a) The band structure of an armchair MoS_2 nanoribbon. All the bands are doubly degenerated due to spin. (b) The ensemble average of the total transmission T as a function of energy for different roughness amplitudes. (c) $T_{\uparrow\uparrow}$ as a function of roughness amplitude for MoS_2 and WS_2. The inset shows $T_{\uparrow\uparrow}$ versus energy for MoS_2. (d) $T_{\uparrow\downarrow}$ as a function of δh for armchair WS_2 and MoS_2 nanoribbons. The inset shows $T_{\uparrow\downarrow}$ versus energy for WS_2. All results for $nW = 15$ and $L = 20$ nm.

to notice that the energy bands are spin degenerated and they are split away from the time-reversal invariant Γ point of the Brillouin zone due to the effect of SOC [52]. The orbital character of each band is shown in Fig. 3. It is interesting to notice that, due to the band-folding characteristic of a nanoribbon, the bands at the Γ point present an important contribution from $d_{3z^2-r^2}$, $d_{x^2-y^2}$, and d_{xy} for both, valence and conduction states. The ensemble average of the total transmission probability for this system is calculated, by using Eq. (7), for several amplitudes of surface roughness with $L_x = L_y = 40$ nm, and the results are shown in Fig. 2(b). In the absence of surface corrugation ($\delta h = 0$) the transmission at a given energy E is equal to the number of available sub-bands at that particular energy. For example, around $E = 0$ we observe that $\langle TE \rangle \approx 4$ for $\delta h = 0$ [blue line in Fig. 2(b)], which corresponds to the contribution of the two pairs of sub-bands observed in Fig. 2(a), which are doubly degenerated due to spin. Therefore we observe that the transmission probability for flat nanoribbons is almost unaffected by the spin-orbit interaction.

Realistic samples, however, present surface roughness that modulates the distance and overlap between atomic orbitals.

This results in local variations of the hopping parameters and break the surface mirror symmetry. As a consequence, the total transmission decreases with the amplitude of the corrugations. This evolution is shown by the arrow in Fig. 2(b), which shows how the average total transmission $\langle TE \rangle$ decreases with the corrugation amplitude δh.

In order to investigate the role of surface roughness on spin transport, the spin-resolved transmission have been calculated: $T_{\uparrow\uparrow}$ and $T_{\uparrow\downarrow}$ are shown in Figs. 2(c)–2(d) as a function of δh for MoS_2 and WS_2. It can be observed that $T_{\uparrow\uparrow}$ [Fig. 2(c)] and $T_{\uparrow\downarrow}$ [Fig. 2(d)] present opposite trend with the amplitude of surface corrugation δh. As expected the spin-conserved transmission $T_{\uparrow\uparrow}$ [like the total transmission $\langle TE \rangle$, Fig. 2(b)] decreases with δh. This behavior is due to the enhancement of the spin-flip processes in Eq. (7) induced by the variation of the hoppings associated to the sample corrugation. In fact $T_{\uparrow\downarrow}$, an indication of spin-flip rate, increases with δh, as shown in Fig. 2(d). Both quantities, $T_{\uparrow\uparrow}$ and $T_{\uparrow\downarrow}$, are larger for WS_2 (diamonds) than for MoS_2 (squares). In particular, $T_{\uparrow\downarrow}$ for WS_2 is approximately an order of magnitude larger than that of MoS_2 [Fig. 2(d)]. This is expected since WS_2 has a larger intrinsic spin-orbit coupling than MoS_2 (see Table I), which
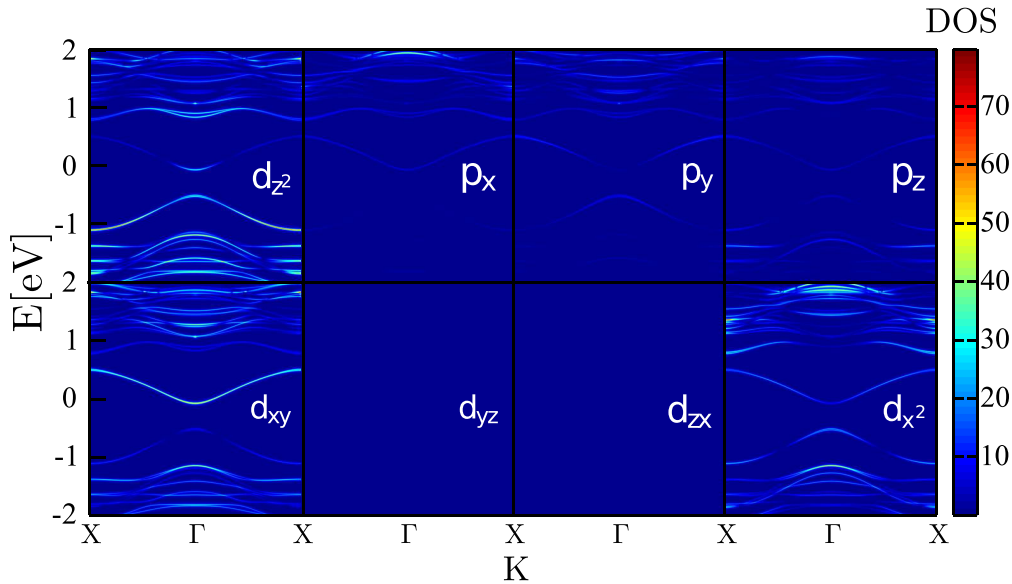
FIG. 3. Orbital character of the band structure of the MoS_2 nanoribbon shown in Fig. 2(a). Each panel represents the orbital weight of the corresponding band, where the labels refer to the d character of Mo atom ($d_{3z^2-r^2}$, d_{xz}, d_{yz}, $d_{x^2-y^2}$, and d_{xy}), and the p character of the chalcogen atom S (p_x, p_y, and p_z). The color scale indicates the corresponding orbital contribution. SOC is not included in this figure.

results in a stronger Rashba-like spin-orbit interaction induced by surface roughness, with the corresponding enhancement of spin-flip processes.

The inset of Fig. 2(d) clearly shows that $T_{\uparrow\downarrow}$ increases exponentially with roughness amplitude of up to four order of magnitude over a variation of δh from $\sim 10^{-2}$ pm to $\sim 10^2$ pm. Interestingly, our calculations also suggest that $T_{\uparrow\downarrow}$ reaches a maximum for a given value of δh, and then it starts to decrease. This threshold is about ≈ 75 pm for MoS_2 and ≈ 100 pm for WS_2 [see Fig. 2(d)]. As explained before two scattering mechanisms affect spin transport: surface corrugation and spin-orbit interaction, which is enhanced with surface roughness. It is also interesting to notice that the spin-flip scattering rate is similar for electron and hole sectors. Since we are dealing with ribbon geometry both, the edge states and the folding of the Brillouin zone, play an important role. In particular, it is very important to notice that the bands [Fig. 2(a)] are spin degenerate (for both, electron and hole sectors) for the armchair nanoribbons considered here. This is completely different to the case of bulk single layer or zigzag nanoribbons [52], where spin-valley coupling is more robust for valence band states, since valence band edges at K and K' valleys correspond to opposite spin, and they are well separated in energy from the other sub-band (the separation is ~ 150 meV for MoS_2 and ~ 400 eV for WS_2). The armchair termination is a line of dimers with atoms of the two sublattices, therefore the edge states present valley mixing, as it happens in graphene armchair ribbons (see, e.g., Refs. [51,53,54]). Furthermore, the orbital contribution for the low-energy states of both, valence and conduction bands, are rather similar, as it can be seen in Fig. 3. This is due to the band folding that happens for a finite ribbon, with the result that, at the Γ point of the ribbon BZ, there are contributions from bulk states at Γ and K points. The consequence of this band reconstruction is that, due to the spin degeneracy of the bands and the similar orbital character for

electron and hole sectors, the spin-flip scattering probability is of the same order in the two cases.

We have considered other kinds of corrugations such as periodic sinusoidal rippling of the sample. We have observed that this kind of corrugation, which can be induced in the laboratory by using elastomeric substrates [55], leads to qualitatively similar effects in the spin-flip transmission $T_{\uparrow\downarrow}$ (not shown here) but of much weaker magnitude as compared to random Gaussian modulation. We have also checked that bending of the ribbon leads to reduction of $T_{\uparrow\downarrow}$ as the curvature radius increases. For this case, the polarized transmission is also much smaller than the obtained with the Gaussian corrugation.

It is interesting to calculate the spin-flip relative transmission (SFRT) $\chi_S = T_{\uparrow\downarrow}/(T_{\uparrow\uparrow} + T_{\uparrow\downarrow})$, which is a measure of the efficiency of spin control [56]. As expected, the ensemble average of χ_S as a function of energy [Fig. 4(a)] increases with surface roughness amplitude. We next compare χ_S for edge and bulk states, as indicated in Fig. 4(b). The amplitude of the edge-state wave functions across the width of the armchair ribbon is originated mainly from d orbitals of the metal (Mo or W) and it is localized at the border atoms, decreasing with the distance to the edge. Our results show that bulk states are strongly affected by surface roughness, whereas edge states are more robust against corrugations, which results in a lower χ_S. This is expected since the spatial localization of edge states protect them partially from surface corrugation effects. The results for transport from purely bulk states are shown in Appendix, where we show simulations with periodic boundary conditions. At high energies and large δh, χ_S reaches 0.5, which implies a complete loss of spin information during transmission. This clearly suggest that substrates with rough surfaces, such as the most commonly used SiO_2, are not appropriate for spintronic applications based on TMDC materials (see Table II).
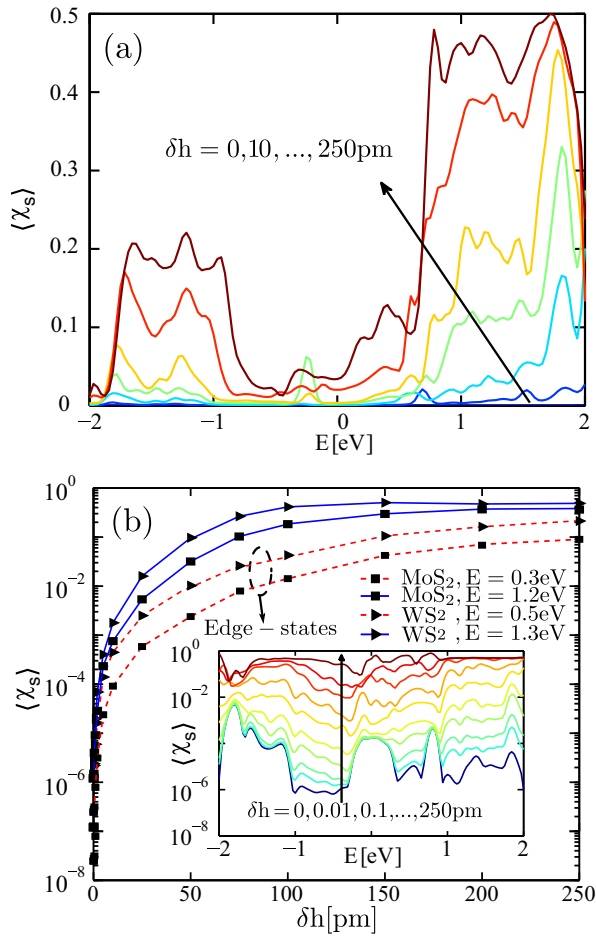
FIG. 4. (a) Spin-flip relative transmission as a function of energy at various roughness amplitudes in armchair MoS$_2$. (b) Spin-flip relative transmission versus δh for both MoS$_2$ and WS$_2$ nanoribbons. The inset shows SFRT in logarithmic scale for WS$_2$. All results for $nW = 15$ and $L = 20$ nm.

FIG. 5. (a) The normalized spin polarized conductance (η) as a function of surface roughness amplitude for MoS$_2$ and WS$_2$ for two different values of Fermi energy. (b) Logarithmic $1 - \eta$ versus logarithmic surface roughness amplitude can better describe the behavior of η for low δh. The inset show η versus Fermi energy at various surface roughness. All results for $L = 20$ nm.

The spin-flip ratio (η) is another important figure of merit for spintronic devices, defined as

$$\eta = \frac{\mathcal{G}_{sc} - \mathcal{G}_{sf}}{\mathcal{G}_{sc} + \mathcal{G}_{sf}}, \qquad (11)$$

where $\mathcal{G}_{sc} = \mathcal{G}_{\uparrow\uparrow} + \mathcal{G}_{\downarrow\downarrow}$ and $\mathcal{G}_{sf} = \mathcal{G}_{\uparrow\downarrow} + \mathcal{G}_{\downarrow\uparrow}$, are the spin-conserving and spin-flip conductances respectively [57]. The conductance in the linear regime is given by [58]

$$\mathcal{G}_{\sigma\sigma'} = \mathcal{G}_0 \int_{-\infty}^{+\infty} dE \left(-\frac{\partial f(E - \epsilon_f)}{\partial E} \right) T_{\sigma\sigma'}(E), \qquad (12)$$

where $\mathcal{G}_0 = e^2/h$, $f(E)$ is the Fermi-Dirac distribution and $T_{\sigma\sigma'}(E)$ is the transmission, Eq. (8). The position of the Fermi level affects the conductance. The results of our calculations are plotted, as a function of roughness amplitudes δh, in Fig. 5 for $\epsilon_f = 0.5$ eV, coinciding with an edge-state band, and for $\epsilon_f = 1.2$ eV, which crosses the bulk bands. The reduction of η with δh suggests again that the spin-flip rate is increased by the surface corrugation. Smaller η is observed for higher values of the Fermi energy. This is due to the smaller effect of corrugations on edge states and to the larger density of states at
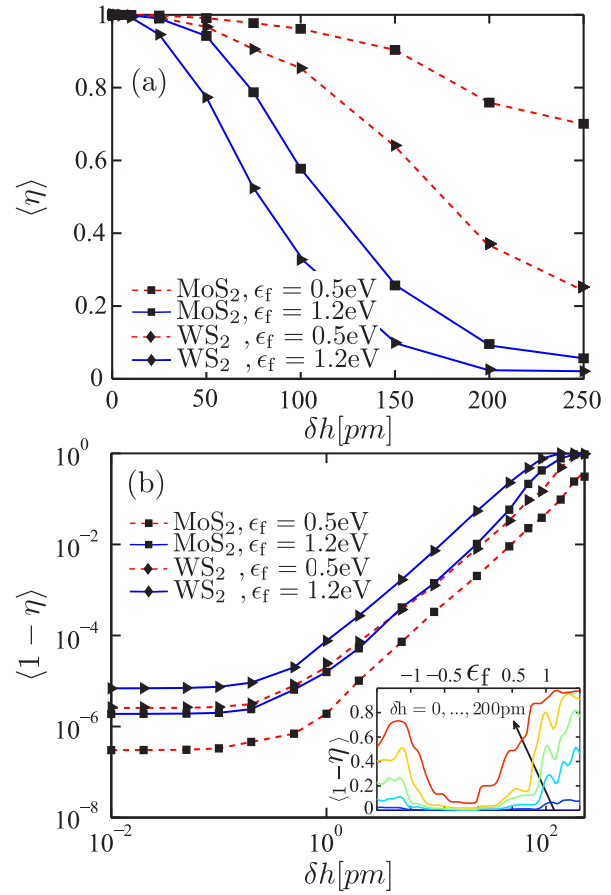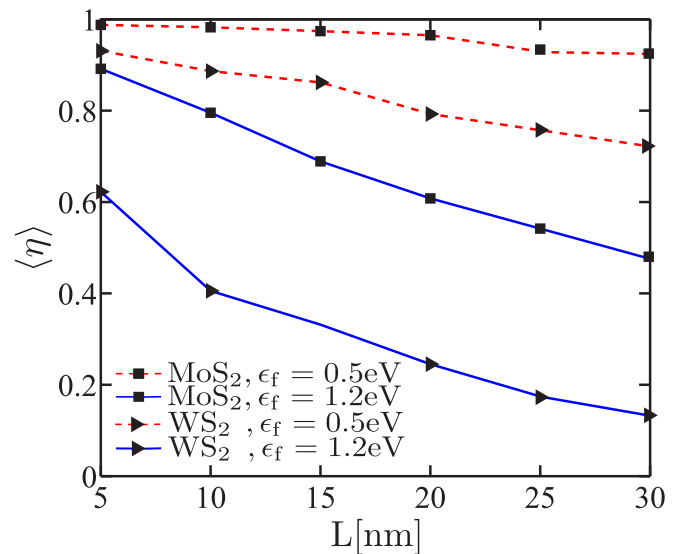

FIG. 6. η as a function of the channel length for MoS$_2$ and WS$_2$ nanoribbons. Results for $\delta h = 100$ pm, $nW = 15$, $L_x = L_y = 50$nm.
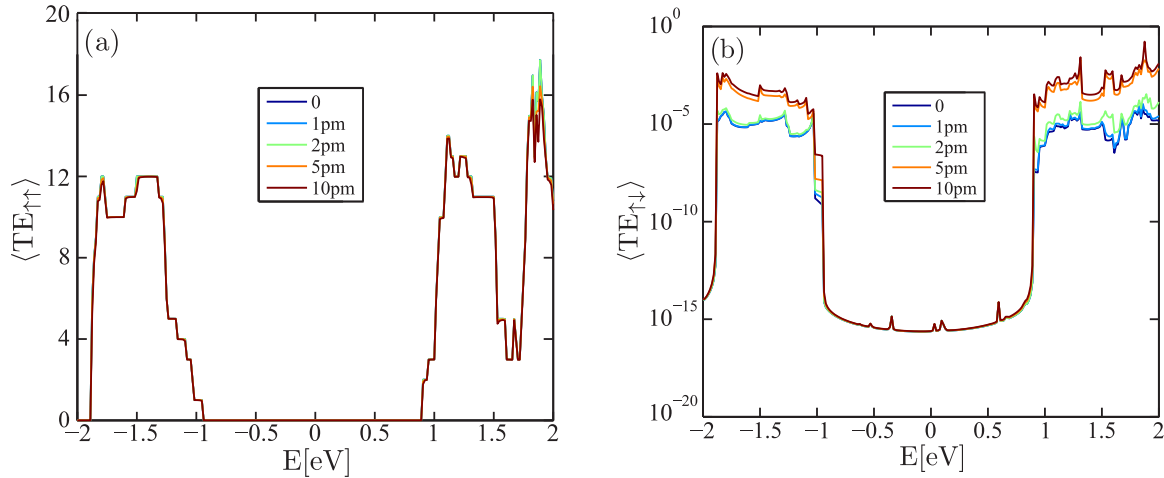
FIG. 7. (a) $T_{\uparrow\uparrow}$ of MoS_2 as a function of energy, using periodic boundary conditions, for different values of δh. (b) Same as (a) but for $T_{\uparrow\downarrow}$. All results for $nW = 15$ and $L = 20$ nm.

high energies, which cause more spin-flip processes. A similar effect has been observed in graphene [38].

Finally, in Fig. 6 we show the dependence of η with the channel length, for the same values of the Fermi energy. We observe that the decay of η with the channel length is more pronounced for $\epsilon_f = 1.2$ eV (crossing bulk states) than for $\epsilon_f = 0.5$ eV (crossing edge states). This can be understood again from the fact that spin transport in the second case occurs mainly through the edges, for which we have seen that the effect of corrugations is small. However, when the Fermi level crosses the bulk states, strongly affected by corrugations, η decreases faster with the length of the channel.

IV. CONCLUSION

In summary, we have performed a systematic theoretical study on spin transport in MoS_2 and WS_2 armchair nanoribbons in the presence of surface roughness. In the perfectly flat ribbons, the spin-flip terms contribution are negligible. Nonetheless, when surface roughness is present, surface mirror symmetry or z-axis symmetry is broken generating an additional Rashba-like contribution to the spin-orbit coupling. The strength of this coupling is proportional to the atomic SOC and increases with the corrugation amplitude. Deformation of the surface by ripples, bending or corrugation, modulates the atomic positions thus changing the atomic interactions and orbital hybridization. The results indicate that sample corrugations significantly enhance the spin-flip rate. For the same surface roughness, the spin-flip rate is larger in WS_2 than in MoS_2 due to the stronger intrinsic SOC of heavier W atoms. Our results indicate that the spin information can be completely suppressed in TMDCs-based channel with

armchair termination supported on rough substrates, such as SiO_2. Therefore, the use of flat substrates or the application of techniques to stretch the MoS_2 or WS_2 samples, avoiding undesirable corrugations, can improve the performance of TMDCs-based spintronics devices.

APPENDIX: SIMULATIONS WITH PERIODIC BOUNDARY CONDITIONS

In order to identify the contribution to transport from purely bulk states, in this Appendix we present results of calculations done with periodic boundary conditions. The results are shown in Fig. 7. Here the amplitude of the corrugations ($\sim$10 pm) is much smaller than the used for open boundary conditions (up to $\sim$250 pm). This is due to a technical difficulty to obtain the same corrugation in the two edges of the nanoribbon to be connected when periodic boundary conditions are considered. Even for such small corrugations, we observe that $TE_{\uparrow\downarrow}$ due to purely bulk states (there is no edge states present in this calculation) increases in more than two order of magnitude from a flat nanoribbon to one with corrugations of $\sim$10 pm amplitude.

[1] W. Han, R. K. Kawakami, M. Gmitra, and J. Fabian, Nature Nanotech. **9**, 794 (2014).

[2] S. Roche, J. Åkerman, B. Beschoten, J.-C. Charlier, M. Chshiev, S. P. Dash, B. Dlubak, J. Fabian, A. Fert, M. Guimarães *et al.*, 2D Mater. **2**, 030202 (2015).

[3] K. S. Novoselov, V. Fal, L. Colombo, P. Gellert, M. Schwab, K. Kim *et al.*, Nature (London) **490**, 192 (2012).

[4] A. Geim and I. Grigorieva, Nature (London) **499**, 419 (2013).

[5] J. Klinovaja and D. Loss, Phys. Rev. B **88**, 075404 (2013).

[6] H. Ochoa and R. Roldán, Phys. Rev. B **87**, 245421 (2013).

[7] N. Zibouche, P. Philipsen, A. Kuc, and T. Heine, Phys. Rev. B **90**, 125440 (2014).

[8] A. Kormányos, V. Zólyomi, N. D. Drummond, and G. Burkard, Phys. Rev. X **4**, 011034 (2014).

[9] K. Kośmider and J. Fernández-Rossier, Phys. Rev. B **87**, 075451 (2013).

[10] T. Georgiou, R. Jalil, B. D. Belle, L. Britnell, R. V. Gorbachev, S. V. Morozov, Y.-J. Kim, A. Gholinia, S. J. Haigh, O. Makarovsky *et al.*, Nature Nanotechnol. **8**, 100 (2013).

[11] S. Lebegue and O. Eriksson, Phys. Rev. B **79**, 115409 (2009).

[12] H. Zeng, G.-B. Liu, J. Dai, Y. Yan, B. Zhu, R. He, L. Xie, S. Xu, X. Chen, W. Yao *et al.*, Sci. Rep. **3**, 1608 (2013).

[13] H. Zeng, J. Dai, W. Yao, D. Xiao, and X. Cui, Nature Nanotechnol. **7**, 490 (2012).

[14] G. Sallen, L. Bouet, X. Marie, G. Wang, C. Zhu, W. Han, Y. Lu, P. Tan, T. Amand, B. Liu *et al.*, Phys. Rev. B **86**, 081301 (2012).

[15] D. Xiao, G.-B. Liu, W. Feng, X. Xu, and W. Yao, Phys. Rev. Lett. **108**, 196802 (2012).

[16] Y. Song and H. Dery, Phys. Rev. Lett. **111**, 026601 (2013).

[17] A. T. Neal, H. Liu, J. Gu, and P. D. Ye, ACS Nano **7**, 7077 (2013).

[18] J. Brivio, D. T. Alexander, and A. Kis, Nano Lett. **11**, 5148 (2011).

[19] H. Ochoa, F. Guinea, and V. I. Fal'Ko, Phys. Rev. B **88**, 195417 (2013).

[20] X. Liu, T. Xu, X. Wu, Z. Zhang, J. Yu, H. Qiu, J.-H. Hong, C.-H. Jin, J.-X. Li, X.-R. Wang *et al.*, Nature Commun. **4**, 1776 (2013).

[21] Q. Li, J. Newberg, E. Walter, J. Hemminger, and R. Penner, Nano Lett. **4**, 277 (2004).

[22] Z. Wang, H. Li, Z. Liu, Z. Shi, J. Lu, K. Suenaga, S.-K. Joung, T. Okazaki, Z. Gu, J. Zhou *et al.*, J. Am. Chem. Soc. **132**, 13840 (2010).

[23] C. Nethravathi, A. A. Jeffery, M. Rajamathi, N. Kawamoto, R. Tenne, D. Golberg, and Y. Bando, ACS Nano **7**, 7311 (2013).

[24] K. Vasu, S. S. Yamijala, A. Zak, K. Gopalakrishnan, S. K. Pati, and C. Rao, Small **11**, 3916 (2015).

[25] Y. Li, Z. Zhou, S. Zhang, and Z. Chen, J. Am. Chem. Soc. **130**, 16739 (2008).

[26] F. López-Urías, A. L. Elías, N. Perea-López, H. R. Gutiérrez, M. Terrones, and H. Terrones, 2D Mater. **2**, 015002 (2015).

[27] E. Cappelluti, R. Roldán, J. A. Silva-Guillén, P. Ordejón, and F. Guinea, Phys. Rev. B **88**, 075409 (2013).

[28] H. Rostami, R. Roldán, E. Cappelluti, R. Asgari, and F. Guinea, Phys. Rev. B **92**, 195402 (2015).

[29] R. Roldán, M. P. Lopez-Sancho, F. Guinea, E. Cappelluti, J. A. Silva-Guillén, and P. Ordejón, 2D Mater. **1**, 034003 (2014).

[30] X. Xu, W. Yao, D. Xiao, and T. F. Heinz, Nature Phys. **10**, 343 (2014).

[31] P.-C. Yeh, W. Jin, N. Zaki, D. Zhang, J. T. Sadowski, A. Al-Mahboob, A. M. van der Zande, D. A. Chenet, J. I. Dadap, I. P. Herman *et al.*, Phys. Rev. B **89**, 155408 (2014).

[32] W. Jin, P.-C. Yeh, N. Zaki, D. Zhang, J. T. Liou, J. T. Sadowski, A. Barinov, M. Yablonskikh, J. I. Dadap, P. Sutter *et al.*, Phys. Rev. B **91**, 121409 (2015).

[33] H. Ochoa, R. Zarzuela, and Y. Tserkovnyak, Phys. Rev. Lett. **118**, 026801 (2017).

[34] M. Pourfath, *The Non-Equilibrium Green's Function Method for Nanoscale Device Simulation* (Springer, Berlin, 2014).

[35] M. P. L. Sancho, J. M. L. Sancho, and J. Rubio, J. Phys. F: Met. Phys. **14**, 1205 (1984).

[36] M. P. L. Sancho, J. M. L. Sancho, and J. Rubio, J. Phys. F: Met. Phys. **15**, 851 (1985).

[37] S. M. Goodnick, D. K. Ferry, C. W. Wilmsen, Z. Liliental, D. Fathy, and O. L. Krivanek, Phys. Rev. B **32**, 8171 (1985).

[38] S. B. Touski and M. Pourfath, Appl. Phys. Lett. **103**, 143506 (2013).

[39] W. A. Harrison, *Elementary Electronic Structure* (World Scientific, Singapore, 1999).

[40] P. San-Jose, V. Parente, F. Guinea, R. Roldán, and E. Prada, Phys. Rev. X **6**, 031046 (2016).

[41] J. Feng, X. Qian, C.-W. Huang, and J. Li, Nature Photon. **6**, 866 (2012).

[42] L. Wang, A. Kutana, and B. I. Yakobson, Ann. Phys. (N.Y.) **526**, L7 (2014).

[43] M. Yamamoto, S. Dutta, S. Aikawa, S. Nakaharai, K. Wakabayashi, M. S. Fuhrer, K. Ueno, and K. Tsukagoshi, Nano Lett. **15**, 2067 (2015).

[44] D. Sercombe, S. Schwarz, O. Del Pozo-Zamudio, F. Liu, B. J. Robinson, E. A. Chekhovich, I. I. Tartakovskii, O. Kolosov, and A. I. Tartakovskii, Sci. Rep. **3**, 3489 (2013).

[45] J. Quereda, A. Castellanos-Gomez, N. Agraït, and G. Rubio-Bollinger, Appl. Phys. Lett. **105**, 053111 (2014).

[46] A. Azcatl, S. McDonnell, K. Santosh, X. Peng, H. Dong, X. Qin, R. Addou, G. I. Mordi, N. Lu, J. Kim *et al.*, Appl. Phys. Lett. **104**, 111601 (2014).

[47] Y. Yu, C. Li, Y. Liu, L. Su, Y. Zhang, and L. Cao, Sci. Rep. **3**, 1866 (2013).

[48] Q. Ji, Y. Zhang, T. Gao, Y. Zhang, D. Ma, M. Liu, Y. Chen, X. Qiao, P.-H. Tan, M. Kan *et al.*, Nano Lett. **13**, 3870 (2013).

[49] D. Huertas-Hernando, F. Guinea, and A. Brataas, Phys. Rev. B **74**, 155426 (2006).

[50] L. Chico, M. P. López-Sancho, and M. C. Muñoz, Phys. Rev. B **79**, 235423 (2009).

[51] M. P. López-Sancho and M. C. Muñoz, Phys. Rev. B **83**, 075406 (2011).

[52] H. Rostami, R. Asgari, and F. Guinea, J. Phys.: Condens. Matter **28**, 495001 (2016).

[53] L. Brey and H. A. Fertig, Phys. Rev. B **73**, 235411 (2006).

[54] S. Yuan, R. Roldán, A.-P. Jauho, and M. I. Katsnelson, Phys. Rev. B **87**, 085430 (2013).

[55] J. Quereda, P. San-Jose, V. Parente, L. Vaquero-Garzon, A. J. Molina-Mendoza, N. Agraït, G. Rubio-Bollinger, F. Guinea, R. Roldán, and A. Castellanos-Gomez, Nano Lett. **16**, 2931 (2016).

[56] P. Michetti, P. Recher, and G. Iannaccone, Nano Lett. **10**, 4463 (2010).

[57] L. Chico, A. Latgé, and L. Brey, Phys. Chem. Chem. Phys. **17**, 16469 (2015).

[58] D. Ryndyk, R. Gutiérrez, B. Song, and G. Cuniberti, *Energy Transfer Dynamics in Biomaterial Systems* (Springer, Berlin, 2009), pp. 213–335.